

RESEARCH ARTICLE

LES of spatially developing turbulent boundary layer over a concave surface

Sunil K. Arolla ^{a*} and Paul A. Durbin^b

^a637 Frank H. T. Rhodes Hall, Sibley School of Mechanical and Aerospace Engineering,
 Cornell University, Ithaca, NY 14853, USA;

^b2237 Howe Hall, Aerospace Engineering, Iowa State University, Ames, IA 50011, USA

(Received 00 Month 200x; final version received 00 Month 200x)

We revisit the problem of a spatially developing turbulent boundary layer over a concave surface. Unlike previous investigations, we simulate the combined effects of streamline curvature as well as curvature-induced pressure gradients on the turbulence. Our focus is on investigating the response of the turbulent boundary layer to the sudden onset of curvature and the destabilizing influence of concave surface in the presence of pressure gradients. This is of interest for evaluating the turbulence closure models. At the beginning of the curve, the momentum thickness Reynolds number is 1520 and the ratio of boundary layer thickness to the radius of curvature is $\delta_0/R = 0.055$. The radial profiles of the mean velocity and turbulence statistics at different locations along the concave surface are presented. Our recently proposed curvature-corrected RANS model is assessed in an *a posteriori* sense and the improvements obtained over the base model are reported. From the LES results, it was found that the maximum influence of concave curvature is on the wall-normal component of the Reynolds stress. The budgets of wall-normal Reynolds stress also confirmed this observation. At the onset of curvature, effect of adverse pressure gradient is found to be predominant. This decreases the skin friction levels below that in the flat section.

Keywords: LES, Turbulence, Concave wall, Streamline curvature, Pressure gradients, Inflow generation, RANS

1. Introduction

A turbulent boundary layer over a concave surface is considered to be a complex flow in that the fluid is subjected to an extra strain rate as well as streamwise pressure gradients. Moreover, centrifugal instability due to concave curvature may induce Taylor-Goertler vortices resulting in large spanwise variations. The early experiments for this configuration are set-up by contouring the opposite convex wall such that a constant pressure is maintained over the concave surface, thus isolating the curvature effects [1, 2]. In a practical configuration, such as flow through high pressure turbines, the blade profile has concave curvature where the effect of curvature cannot be isolated from the curvature-induced streamwise pressure gradients. Hence, understanding the combined effects of curvature and pressure gradients is critical for assessing the turbulence models used in applied CFD.

Barlow and Johnston [3], Johnson and Johnston [4] conducted laboratory experiments using a water channel where a straight entry flow section is connected to a 90° constant radius curvature bend. The convex wall deviates from a circular arc to minimize the streamwise pressure gradient on the concave wall. Lund and

*Corresponding author. Email: ska62@cornell.edu

Moin [5] performed LES simulations using a geometry designed to match these experimental conditions and compared velocity statistics for several streamwise stations. They have reported some discrepancies in the LES results when compared with the experimental data. The results improved when they used parallel flow inflow generation instead of using inflow data from a precursor boundary layer simulation. The concave curvature enhances turbulence and hence the skin friction increases from its value on the flat plate section. In these experiments, the skin friction is only inferred from the velocity measurements by assuming an equilibrium turbulent boundary layer. Hence, LES predicted skin friction did not show good agreement with the data. This LES data has been used to test our recently proposed curvature-corrected RANS models [6]. Our models showed qualitatively correct behavior, but there were quantitative discrepancies.

Combined effects of favorable pressure gradient and streamline curvature on uniformly sheared turbulence were investigated experimentally by Holloway *et al.* [7]. Streamwise pressure gradients were applied by convergence of the curved tunnel walls in the mean shear plane. They showed that the addition of favorable pressure gradient diminishes the turbulence energy and stresses below what it would be under the influence of curvature alone. Flow on uniformly curved surface with pressure gradient has been studied by Schwarz *et al.* [8]. Boundary layer development in an S-shaped duct has been studied by Bandyopadhyay and Ahmed [9], Laskowski and Durbin [10], and Lopes *et al.* [11]. As discussed before, such ducted flow configurations introduce artificially enhanced streamwise coherence and hence show clearly identifiable Taylor-Gortler vortices as also shown by Moser and Moin [12]. In the context of turbomachinery, the focus of the work reported in the literature has been primarily on studying the effects of concave curvature on laminar-to-turbulence transition [13–15], and on studying the Goertler instability (for example, [16] and references there in). To our knowledge, no such detailed studies have been reported on the combined effects of concave curvature and adverse pressure gradients in a boundary layer setting.

In our recent work, we proposed a curvature-corrected RANS modeling framework [6] and showed that the models capture correct trends for both convex and concave wall turbulent boundary layers. The models have also been tested on a stationary serpentine channel configuration which has both convex and concave walls. Concave boundary layer combined with curvature-induced streamwise pressure gradient forms another useful problem to test the reliability of our proposed models. The work reported in this paper is motivated by this need to generate a dataset that can be used for assessing the RANS models with a simple flow configuration.

The research questions addressed in this article are:

- What is the role of adverse pressure gradient at the onset of concave curvature on the flow development ?
- What is the effect of streamwise pressure gradient on the turbulence characteristics over the concave surface ?
- How do the recently proposed curvature-corrected RANS models behave in such a flow configuration ?

To this end, we use a geometry with concave surface of constant radius of curvature and without modifying the opposite wall from its circular arc. LES simulations are performed using a simple variant of recycling and rescaling method of inflow turbulence generation [17]. The inflow data are generated from a precursor flat plate turbulent boundary layer simulation. The rescaling algorithm used in this work is based on momentum thickness and it does not require decomposition of

velocity field into mean and fluctuating components. The outer layer scaling is used throughout and hence no composite formulas are required. Also, there is no need to iterate for obtaining required momentum thickness at the inflow boundary.

In this paper, detailed analysis of the statistics obtained over the curved surface are presented. Our recently proposed curvature-corrected RANS closure models are evaluated followed by a brief discussion on the accuracy of the models.

2. Computational framework

The computational framework used in this research is that of OpenFOAM finite volume based incompressible flow solver. The filtered Navier-Stokes equations solved in the context of LES are:

$$\partial_i \hat{u}_i = 0 \quad (1)$$

$$\partial_t \hat{u}_i + \partial_j \hat{u}_j \hat{u}_i = -\frac{1}{\rho} \partial_i \hat{p} + \nu \nabla^2 \hat{u}_i - \partial_i \tau_{ij}^{SGS} \quad (2)$$

where \hat{u}_i is the filtered velocity field. The unclosed term that arises due to filtering operation are the subgrid scale stresses given by τ_{ij}^{SGS} . The equations are closed by employing a dynamic Smagorinsky model [18] with modification by Lilly [19].

For the LES simulations presented in this article, Pressure Implicit with Splitting of Operator (PISO) algorithm is employed. A second order accurate backward implicit scheme for time discretization and a second order central scheme (with filtering for high-frequency ringing) for spatial discretization is used.

2.1. Inflow turbulence generation: a variant of recycling and rescaling method

The recycling and rescaling method presented in this paper is based on the work by Spalart *et al.* [20] to simplify the inflow generation algorithm using the following physical arguments:

- The near-wall turbulence regenerates itself much faster than the outer region turbulence → Apply outer layer scaling throughout.
- When the recycling station is located quite close to the inflow, which is desirable in terms of computing cost, the conflict between inner and outer region scaling essentially vanishes → Short recycling distance
- Corrections to the wall normal velocity component v have very little effect → Omitted

In the current work, momentum thickness based scaling is used in place of 99% boundary layer thickness. This avoids the need of locating the edge of the boundary layer. Moreover, using integral quantities like momentum thickness (or displacement thickness) is numerically robust. Most experiments report the momentum thickness Reynolds number at the inflow and hence back-to-back simulations can be set-up easily. A spanwise mirroring method [21] is adopted as it was found to be adequate in the current work for disorganizing unphysical spanwise durable structures. It should be noted that more advanced strategies like random-walk based dynamic shifting and reflection might be more efficient, but those have not been tried out in the present work. The detailed steps involved in this method are given in appendix A.

2.2. Flat plate turbulent boundary layer

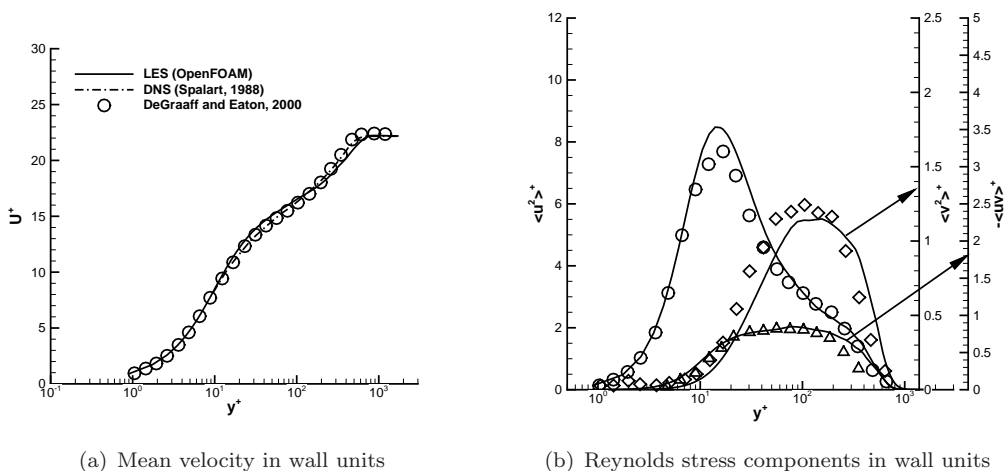


Figure 1. LES of spatially developing flat plate turbulent boundary layer: one-point statistics

As a baseline validation, results from LES of flat plate turbulent boundary layer with inflow momentum thickness Reynolds number of $R_\theta = 1520$ are presented. The computational domain has dimensions $12\delta_0 \times 3\delta_0 \times 3\delta_0$ in the streamwise, wall-normal, and spanwise directions, respectively where δ_0 is the 99% boundary layer thickness at the recycling plane. The mesh contains $182 \times 96 \times 164$ points in the streamwise, wall-normal, and spanwise directions, respectively. In terms of the wall units, the mesh resolution is $\Delta x^+ \approx 45$, $\Delta y_{wall}^+ \approx 1$, $\Delta y_{max}^+ \approx 20$, and $\Delta z^+ \approx 12$. Uniform mesh is used in the streamwise and spanwise directions while a hyperbolic tangent stretching is used in the wall-normal direction to cluster points close to the wall. The recycling station was located at $5\delta_0$ downstream of the inlet and the simulation provides its own inflow. The bottom wall is treated as a no-slip wall, top boundary is a slip wall, and at the outflow an advective boundary condition is used.

As noted in Spalart *et al.* [20], the initialization is important when using such inflow generation algorithms. The mean velocity profile given by Spalding law with random fluctuations with a maximum amplitude of 10% of the freestream value superimposed on the mean value. The time step used is approximately two viscous time units ($\Delta t \approx 2\nu/u_\tau^2$). The simulation was run for 1000 inertial timescales (δ_0/U_∞) to eliminate transients and the statistics are collected over another 1000 timescales.

Figure 1 presents comparison of the mean streamwise velocity and three Reynolds stresses plotted in wall units with the experimental data of DeGraaff and Eaton [22] for a flat plate boundary layer at $R_\theta = 1430$. The mean velocity profile is in good agreement with the experimental profile as well as the DNS of Spalart [23]. The normal Reynolds stresses also show good agreement for the current grid resolution chosen. The shear stress shows much better agreement than that published in the earlier literature with LES.

3. Flow configuration of concave wall boundary layer

Unlike in the previous investigations, the flow configuration used in this work has a concave surface with the top, convex wall not deviating from the circular arc. The specific reason for the chosen geometry is to investigate the combined effects

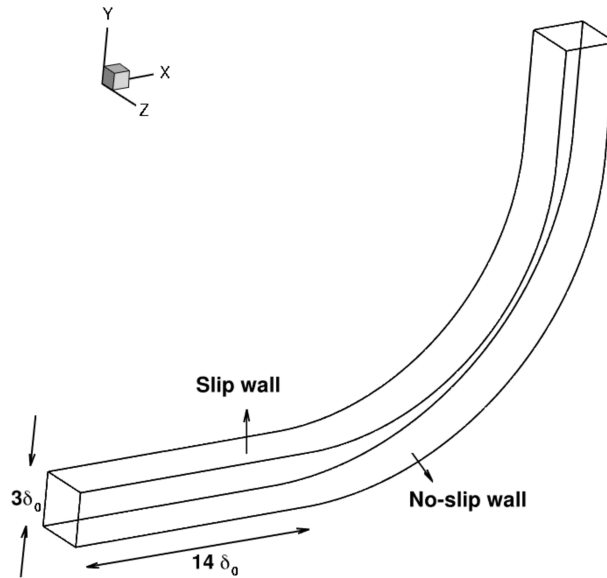


Figure 2. Concave boundary layer: Flow configuration and boundary conditions

of concave curvature and adverse pressure gradients which has not been studied in detail before. The other reason is that such a geometry is easy to reproduce for evaluating turbulence closure modeling ideas. The momentum thickness Reynolds number at the beginning of the curve is $R_{\theta_0} = 1520$ and the ratio of boundary layer thickness to the radius of curvature at this station is $\delta_0/R = 0.055$ which is sufficiently large to see significant curvature effects on the turbulence.

The computational domain is shown in the figure 2. The calculation begins approximately $14\delta_0$ upstream of the concave curvature and the curved section ends at 90° . Time-varying inflow data are generated using a stand-alone flat plate boundary layer simulation using a variant of recycling and rescaling method as discussed in section 2.2. An outflow buffer region is placed at approximately $3\delta_0$ from the end of curved section, called buffer region. This is, essentially, to dissipate large eddies and avoid them from hitting the outflow boundary and reflecting into the flow domain. The domain extends $3\delta_0$ both in the wall-normal and spanwise directions. The concave surface is treated as a no-slip wall and the convex wall is treated as slip boundary. Mean ambient pressure is specified at the outflow. The mesh contains $434 \times 96 \times 164$ points in the streamwise, wall-normal, and spanwise directions, respectively. In terms of the wall units, mesh resolution is $\Delta x^+ \approx 63$, $\Delta y_{wall}^+ \approx 1$, $\Delta y_{max}^+ \approx 20$, and $\Delta z^+ \approx 12$. The flow is initialized using a mean turbulent velocity profile superimposed with fluctuations. The simulation was run for 120 inertial timescales (δ_0/U_∞) to eliminate transients and for another 875 timescales to collect statistics reported in this article.

In such simulations, the particular choice of spanwise domain size is important and deserves some discussion. In a recent work, Schrader *et al.* [16] found that there are a wide range of unstable spanwise wave numbers that trigger Goertler instability. Our spanwise period of $3\delta_{99}$ is within the range of these unstable wave numbers. Moreover, Lund and Moin (1996) [5] found that a spanwise period of $2\delta_{99}$ is sufficient to capture the Taylor-Goertler vortices when they used parallel flow inflow. The sensitivity of these coherent structures to the type of inflow is well established. They are weak or absent for the present case of an inlet turbulent boundary layer. Since our focus is on evaluating RANS closure models, absence of strong Goertler vortices is an advantage over the experiments with screens and boundary layers that go through transition.

4. Results and Discussion

In this section, the mean flow statistics obtained from LES are discussed in detail. The focus of this work is primarily to generate statistics that can be used for RANS model evaluation and hence the coherent structure identification is only briefly discussed.

4.1. Mean flow characteristics

Figure 3 presents the mean velocity profile at different streamwise locations. The first station is on the flat section, approximately five boundary layer thicknesses ahead of the curvature. The second station is at the onset of the concave curvature and remaining four stations are at 15° , 30° , and 60° into the curved section. The velocity is normalized with the freestream velocity and the wall-normal coordinate is normalized with inlet boundary layer thickness. The shape of the velocity profile changes from flat section to the 60° , due to concave curvature. The destabilizing influence of concave curvature enhances mixing of high momentum fluid away from the wall with the slow moving fluid close to the wall and hence the profile looks fuller as one moves downstream.

The Reynolds stress components are plotted in figure 4. The effect of curvature on the streamwise velocity fluctuation is not distinguishable. The wall-normal and spanwise components are enhanced due to the concave curvature. The maximum effect is seen in the wall-normal fluctuations, as expected. The shear stress profiles also show similar behavior. A bulge develops in the central portion of each profile plotted within concave curve. This could be due to centrifugal instability. Such deterministic processes are known to be difficult to reproduce with a RANS based statistical closures and hence this flow configuration remains a challenge problem for such models.

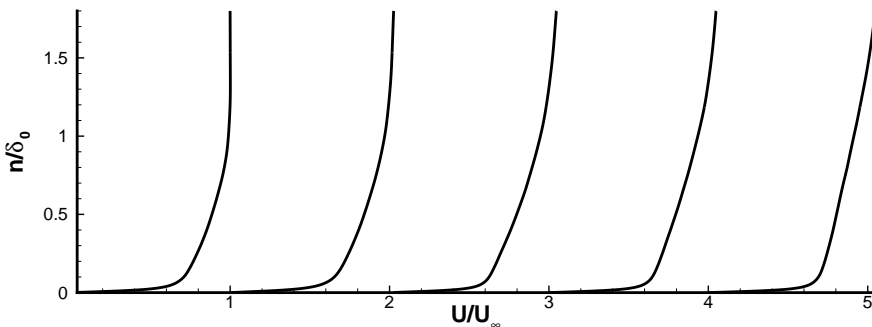
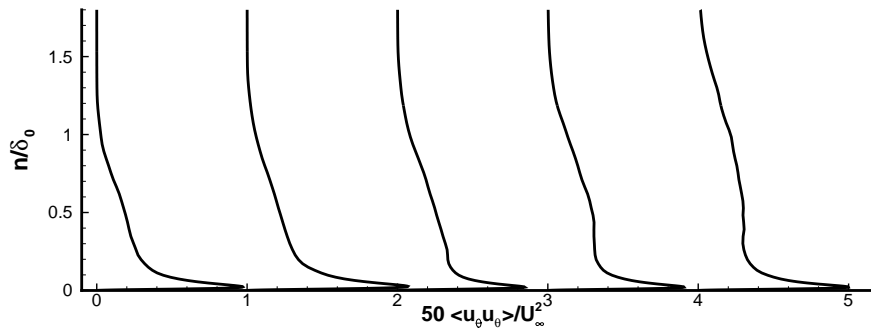
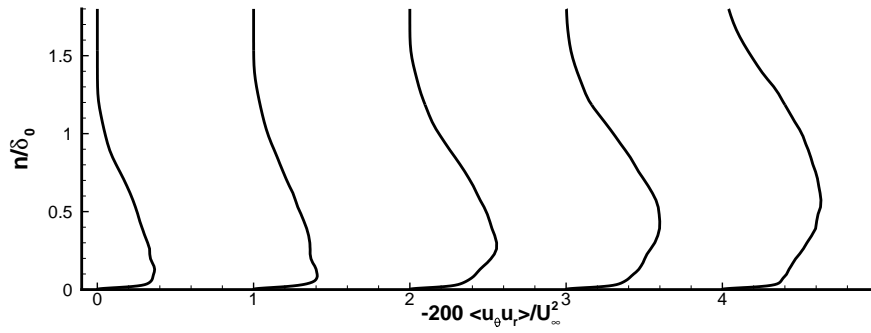


Figure 3. Concave boundary layer: Mean streamwise velocity profiles plotted in wall-normal coordinate normalized by 99% boundary layer thickness at the inflow.

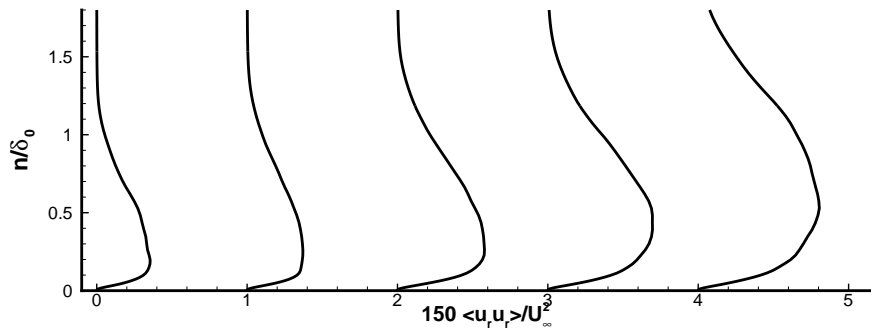
The skin friction and pressure coefficient calculated from LES are plotted in figure 5. The skin friction drops at the onset of curvature due to flow deceleration. This is consistent with the pressure coefficient showing a sudden rise at the onset. The destabilizing influence of concave curvature enhances turbulence and hence the skin friction raises above its value at the onset as the flow moves into the concave section. Close to the outflow boundary, the flow accelerated for recovering to the atmospheric pressure and hence there is a slight increase in skin friction and decrease in the pressure coefficient. The reference pressure used in calculating the pressure coefficient is the pressure at a flat section approximately five boundary layer thicknesses ahead of the curvature. These trends in skin friction and pressure



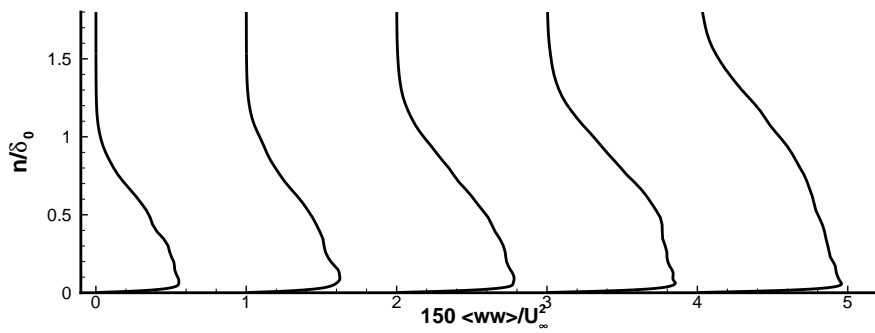
(a) Reynolds stress in wall units: Streamwise component



(b) Reynolds stress in wall units: Shear stress component



(c) Reynolds stress in wall units: Wall-normal component



(d) Reynolds stress in wall units: Spanwise component

Figure 4. Spatially developing concave wall turbulent boundary layer: one-point statistics plotted in streamline coordinates

coefficient agree well with that reported in DNS and LES studies of curved channels [10]. The simulations reported by Lund and Moin [5] are clearly different as they have maintained nearly zero pressure gradient on the concave surface. This is different from our work and hence we see a different behavior in our predicted skin friction.

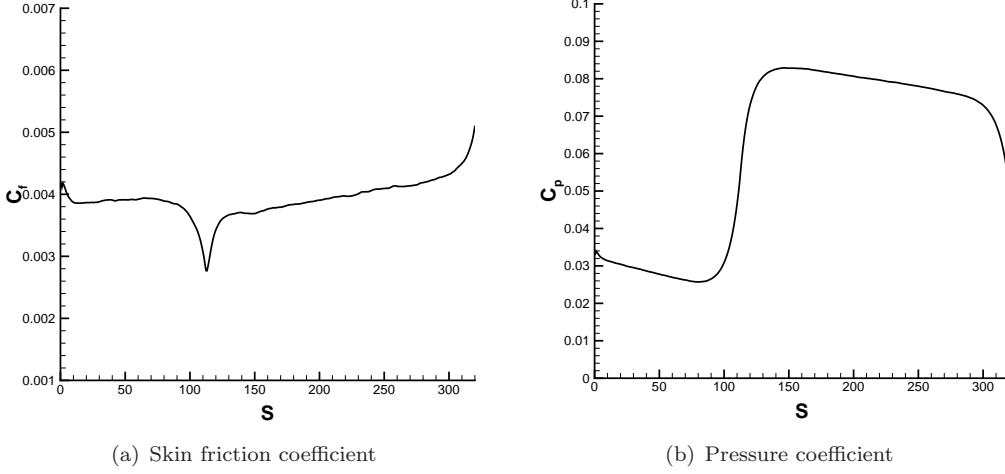


Figure 5. Concave wall boundary layer: Streamwise variation of global quantities of interest to the aerodynamic designers. Here, S is the streamwise distance along the curved surface.

4.2. Turbulent kinetic energy budget analysis

With the pressure-velocity interaction terms decomposed into pressure-strain and pressure-diffusion fragments, the budgets of Reynolds shear stress may be written as:

$$\frac{D\overline{u_i u_j}}{Dt} = P_{ij} - \varepsilon_{ij} + T_{ij} + \Phi_{ij} + D_{ij} + V_{ij}; \quad (3)$$

$$P_{ij} = -\overline{u_j u_k} \frac{\partial U_i}{\partial x_k} - \overline{u_i u_k} \frac{\partial U_j}{\partial x_k}; \quad \varepsilon_{ij} = 2\nu \overline{\frac{\partial u_i}{\partial x_k} \frac{\partial u_j}{\partial x_k}}; \quad T_{ij} = -\frac{\partial \overline{u_i u_j u_k}}{\partial x_k};$$

$$\Phi_{ij} = \frac{p}{\rho} \left(\frac{\partial u_i}{\partial x_j} + \frac{\partial u_j}{\partial x_i} \right); \quad D_{ij} = -\frac{\partial}{\partial x_k} \left(\frac{1}{\rho} \overline{p u_j} \delta_{ik} + \frac{1}{\rho} \overline{p u_i} \delta_{jk} \right); \quad V_{ij} = \nu \frac{\partial^2 \overline{u_i u_j}}{\partial x_k \partial x_k};$$

where P_{ij} , ε_{ij} , T_{ij} , Φ_{ij} , D_{ij} , and V_{ij} are production, dissipation, turbulent transport, pressure-strain, pressure diffusion, and viscous diffusion terms respectively.

The turbulent kinetic energy (TKE) budgets are plotted in the flat section approximately five boundary layer thicknesses upstream of the concave curvature in figure 6. The TKE budget terms are obtained by taking half the trace of equation 3. The production and dissipation attain their largest value close to the wall around $y^+ \approx 12$, and they are unequal. Due to the no-slip boundary condition, production vanishes at the wall. The dissipation, however, is non-zero and has a sharp maximum at the wall. The pressure-strain correlation term has a role of redistributing the energy and has zero trace. The pressure diffusion term is very small. The viscous diffusion and dissipation are equal and opposite at the wall. These are consistent with the observations from DNS of flat plate turbulent boundary layer.

The TKE budgets are plotted at the onset, 15° , 30° , and 60° in figure 7. At the onset of curvature, the terms in the budget do not show much difference from that in the flat plate section except for the turbulent transport. As the flow goes into the concave curvature, the turbulent transport and pressure diffusion terms show higher positive peak close to the wall. The production term shows slight decrease at 15° and then increases at the other two locations. Some of these observations are consistent with that seen in the DNS of curved channel [12]. This is in accordance with Bradshaw's assertion [24] that the curvature effects must appear in the higher-order statistical correlations.

The maximum influence of curvature is on the wall-normal component of Reynolds stress tensor. So, budgets of this component are plotted in figure 8. It clearly shows the enhancement of the production term due to concave curvature. This justifies our approach of correcting the eddy viscosity coefficient to introduce curvature effects within RANS modeling framework. It will be discussed further in section 5.

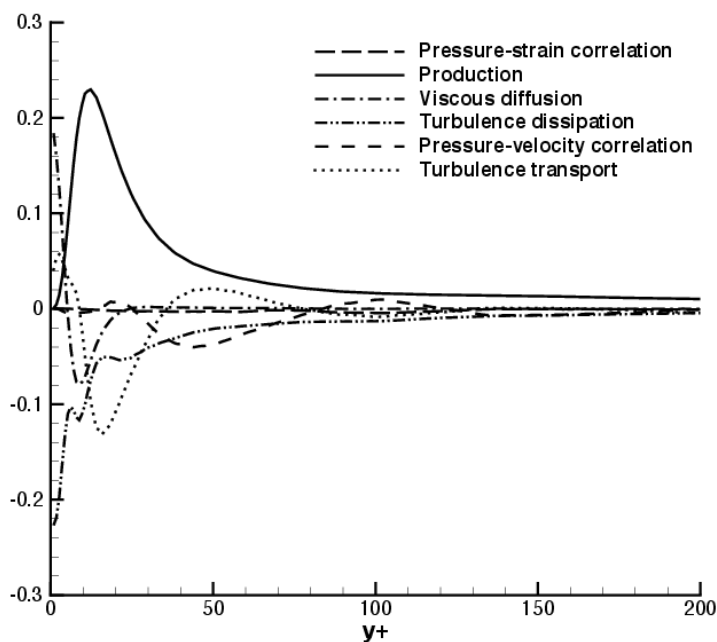


Figure 6. TKE budgets: flat section

4.3. Response to the sudden onset of curvature

At the beginning of the concave wall, the geometric curvature changes as a step function, but the potential flow effects influence a short region upstream and downstream of the start of the geometric curvature. So, the effective curvature felt by the outer layer changes gradually through this region. In agreement with the experimental observations in Barlow and Johnston [3], the greatest changes in the profiles of mean velocity and Reynolds stress components occur downstream of the geometric curvature as shown in figure 4.

At the onset of curvature, the flow is subjected to adverse pressure gradient in the streamwise direction which can be equated to the streamwise deceleration, $U_\infty(dU_\infty/dS)$ where U_∞ is the velocity at the edge of the boundary layer, and S is the distance along the curved surface. The adverse pressure gradient has an effect of

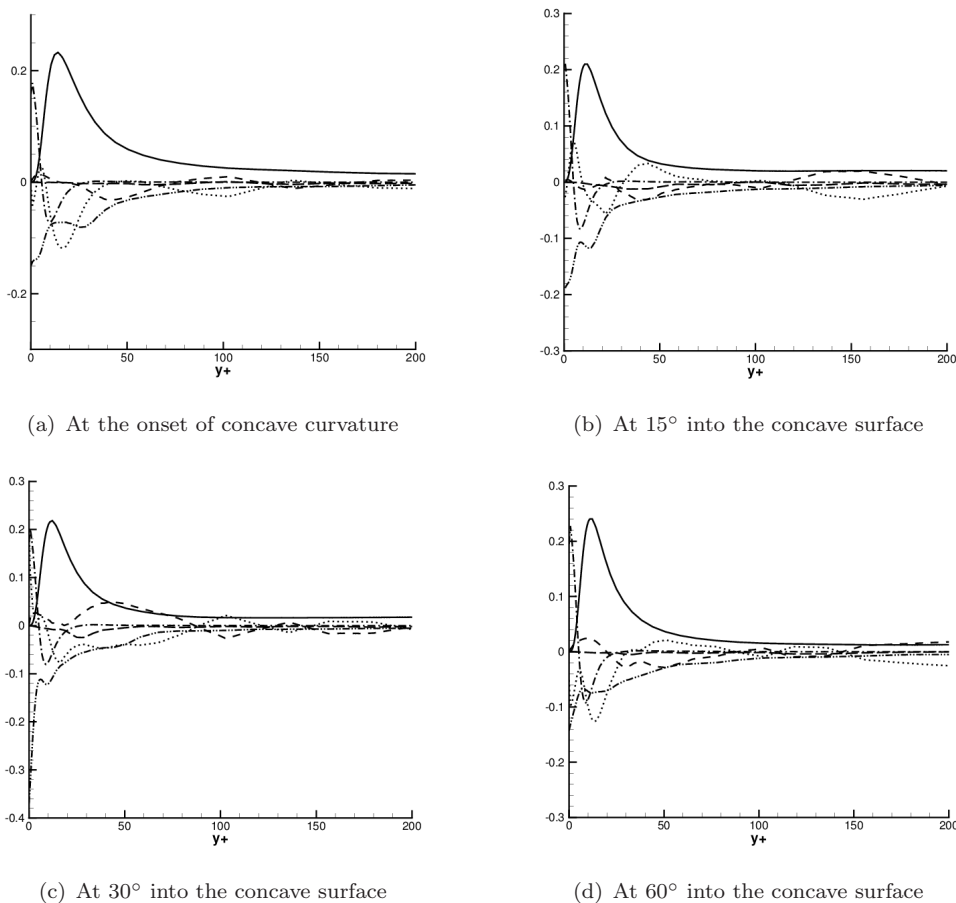


Figure 7. Spatially developing concave wall turbulent boundary layer: Budget of TKE. Here, $y^+ = nu_\tau/\nu$. For line legend, see figure 6.

reducing the skin friction levels and the concave curvature has an effect of enhanced the skin friction levels. There is a competition between these two mechanisms and from the figure 5, the pressure gradient seems to have a dominant influence at the onset of curvature. So, the net effect is a reduction in skin friction. So, if the adverse pressure gradient is strong enough, there is a possibility of incipient flow separation. This is consistent with the observations from earlier DNS and LES of curved channels [10, 11]. This influence of pressure gradient is not distinguishable in the mean velocity or the turbulence quantities plotted at the onset of curvature.

4.4. Coherent structures

The concave curvature may induce Taylor-Goertler vortices due to the centrifugal instability. The existence of these streamwise oriented structures has been questioned [25], but it is well established that concave curvature amplifies disturbances present in the incoming flow, resulting in the formation of roll cells [3]. Depending on the streamwise coherence of the incoming flow, these structures are random in space and time, and can be quite diffuse. They are also limited in streamwise extent making it harder to visualize in a numerical simulation like ours. Lund and Moin [5] verified that using inflow conditions with high degree of streamwise coherence can show formation of stronger vortices.

To determine the presence of Taylor-Goertler vortices, following Moser and Moin [12], a velocity field is defined $\tilde{u}_i(t, n, z)$ by averaging $[\bar{u}_i(t, s, n, z) - U_i(s, n)]$ in the

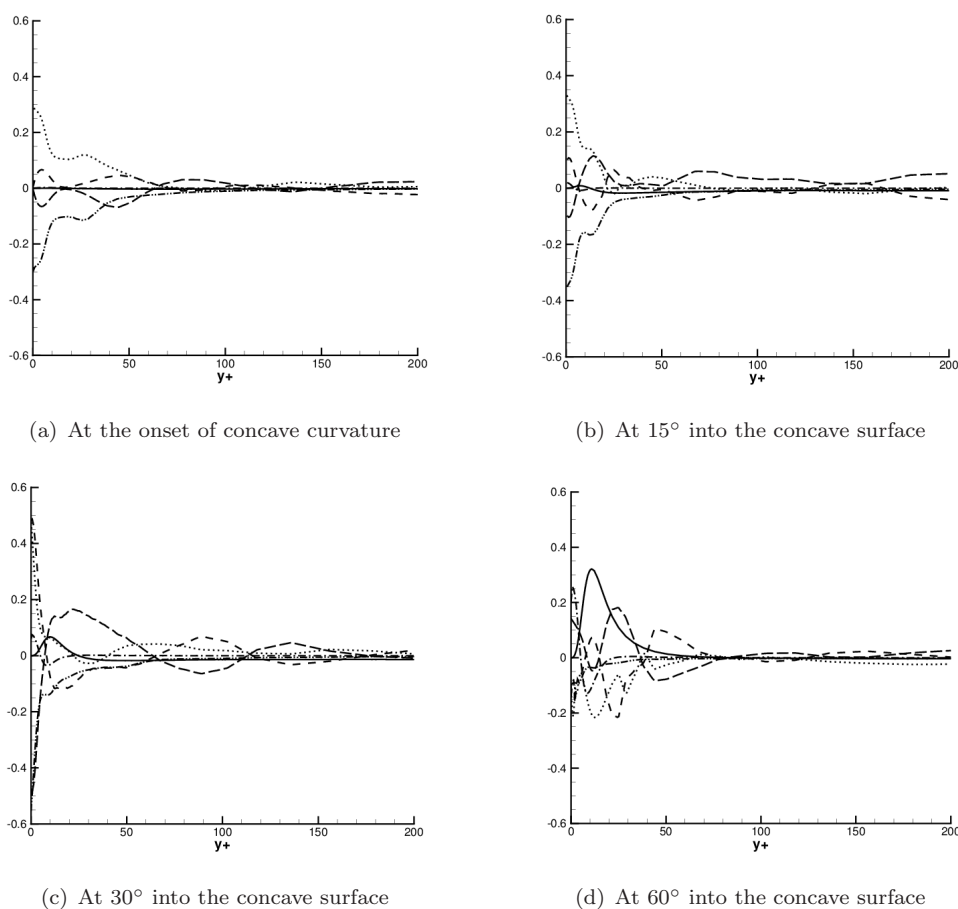


Figure 8. Spatially developing concave wall turbulent boundary layer: Budget of $\langle u_r u_r \rangle$ component. Here, $y^+ = nu_\tau/\nu$. For line legend, see figure 6.

streamwise direction from 15° to 60°, to remove the turbulent motions not due to streamwise-aligned structures. The resulting secondary velocity field is plotted as a cross-plane streamtaces in figure 9. We did not observe coherent structures as in the simulations with parallel-flow inflow data, but some large scale inflows and outflows were observed that are responsible for the enhanced mixing. This explains the reason why there is large increase in the turbulence quantities plotted in figure 4.

Figure 10 shows the vortical structures identified using Q-criterion (second invariant of velocity gradient tensor). The vortical structures are amplified as they move into the concave curvature due to enhanced turbulence levels. These structures are dampened towards the exit due to a coarser grid (buffer zone) used in our simulation set-up.

4.5. Anisotropy invariant map

Figure 11 shows anisotropy invariant map plotted within the Lumley triangle. The quantities plotted are:

$$6\eta^2 = A_2/4; \quad 6\xi^3 = A_3/8 \quad (4)$$

where $A_2 = a_{ij}a_{ji}$, $A_3 = a_{ij}a_{jk}a_{ki}$, with the anisotropy tensor defined as

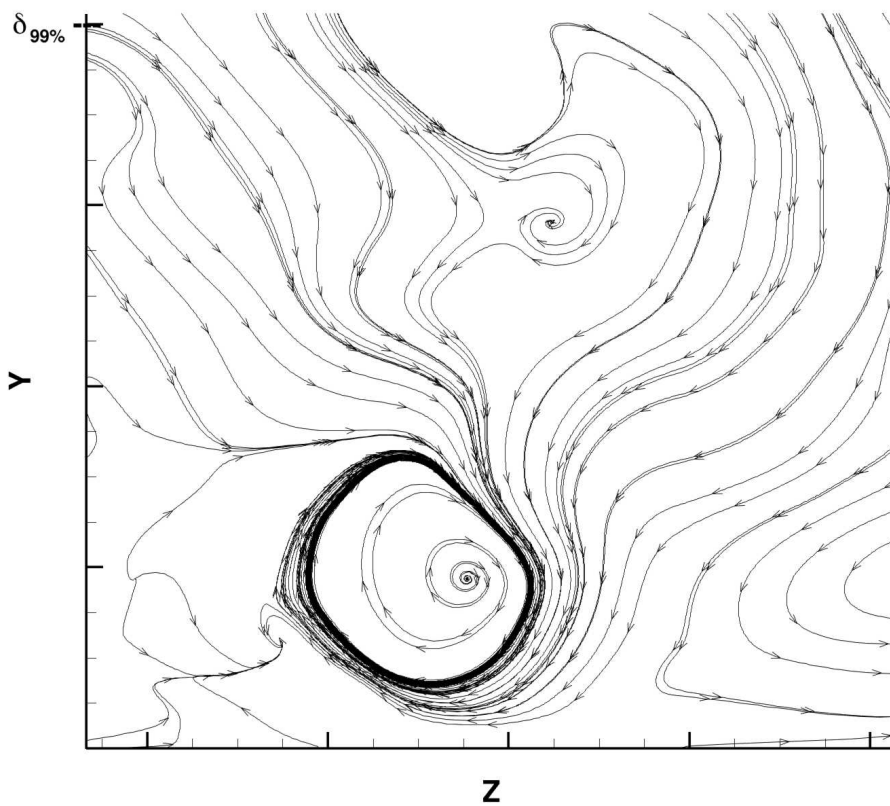


Figure 9. Visualization of large scale inflows and outflows responsible for the transport of high momentum fluid down towards the wall resulting in enhanced mixing. Plotted are the cross-plane streamtraces of the velocity fluctuations averaged in the streamwise direction from 15° to 60° .

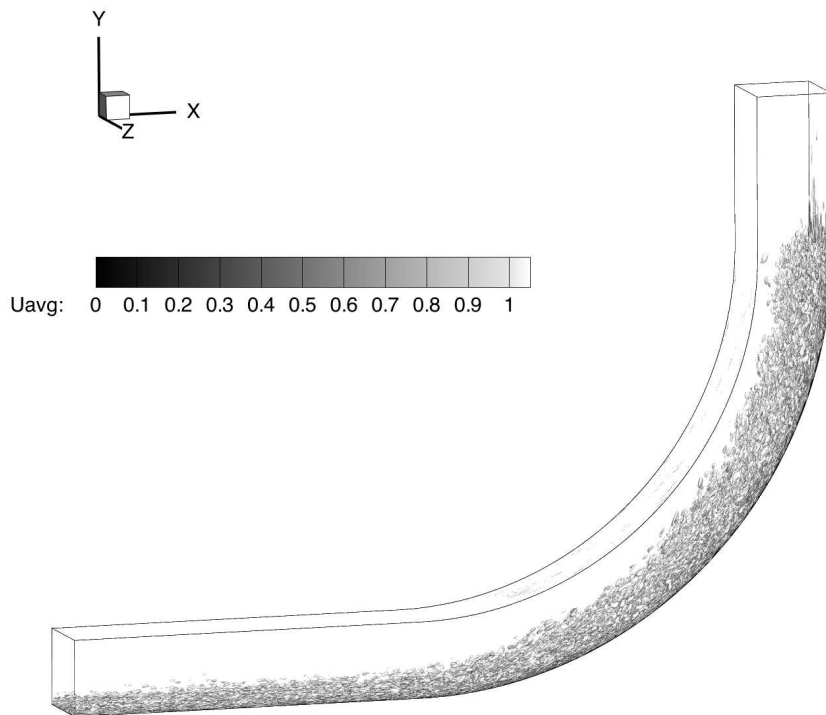


Figure 10. Vortical structures as identified by Q isosurfaces, with $Q = |\Omega|^2 - |S|^2 = -0.01$.

$$a_{ij} = \frac{\overline{u_i u_j}}{k} - \frac{2}{3} \delta_{ij}.$$

The invariant map shows that the turbulence field approaches a two-component state close to the wall and away from the wall, the turbulence tends to move towards isotropic state. The path in which turbulence moves towards isotropic state is different as the flow goes into the concave curvature. In particular, large negative values of third invariant of anisotropy are observed at 30° and 60° which is perhaps due to the bulge observed in the Reynolds stress profiles plotted in figure 4.

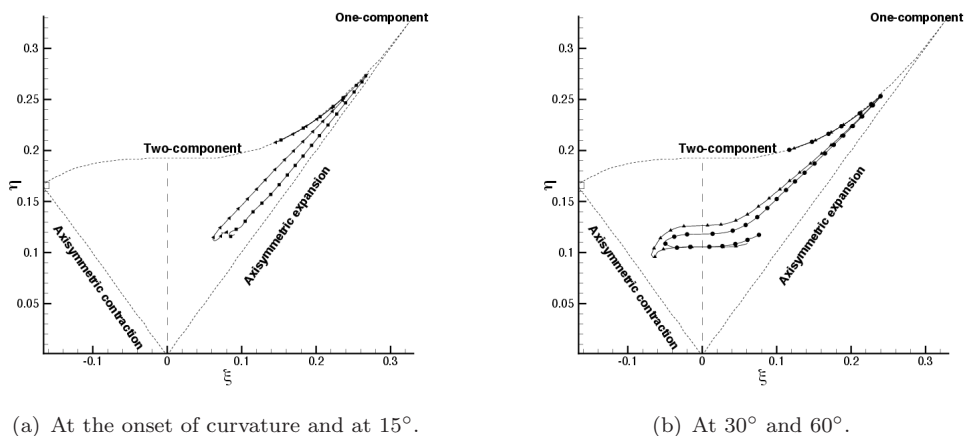


Figure 11. Anisotropy invariant map, plotted below $y^+ \approx 500$.

5. Evaluating curvature-corrected RANS models

Curvature-corrected RANS models proposed in our recent work [6] were evaluated on this problem using the data generated from LES. The baseline turbulence model and curvature correction model are summarized in appendix B.

The inflow data are generated using the same algorithm used for the LES, given in appendix A. The mean velocity profile at the flat section using RANS-type grid resolution is compared with the LES and experimental data in figure 12. This demonstrates that RANS simulations are set-up to be consistent with the LES.

The skin friction and pressure coefficient from RANS computation are plotted in the figures 13. The bifurcation analysis based curvature model shows significant improvement over the base turbulence model. RANS models, in general, overpredict the deceleration at the onset of concave curvature. This remains as an open problem for the RANS models. The percentage raise in the skin friction from that at the onset is predicted accurately by the curvature-corrected RANS model. The mean velocity profiles plotted in figure 14 show only minor differences among different models.

6. Concluding remarks

LES of concave wall turbulent boundary layer with particular focus on combined effects of pressure gradients and curvature is presented. The following are the spe-

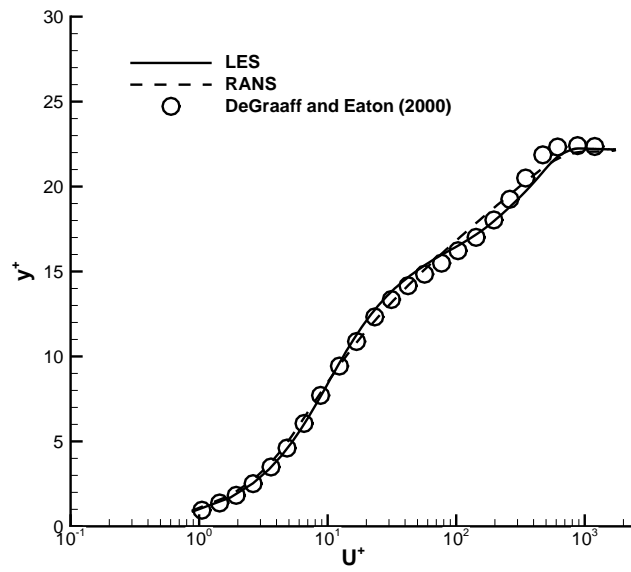


Figure 12. Inflow generation for RANS

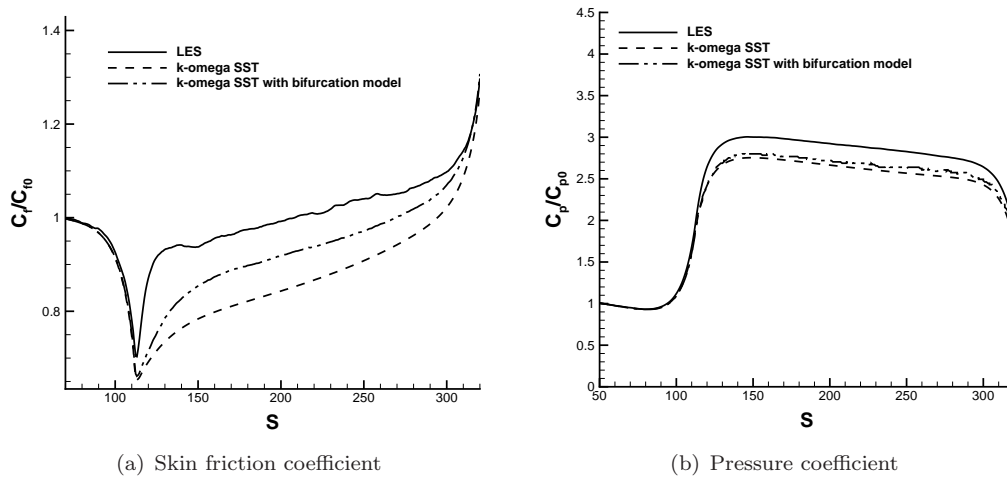


Figure 13. Concave wall boundary layer: Streamwise variation of global quantities of interest to the aerodynamic designers

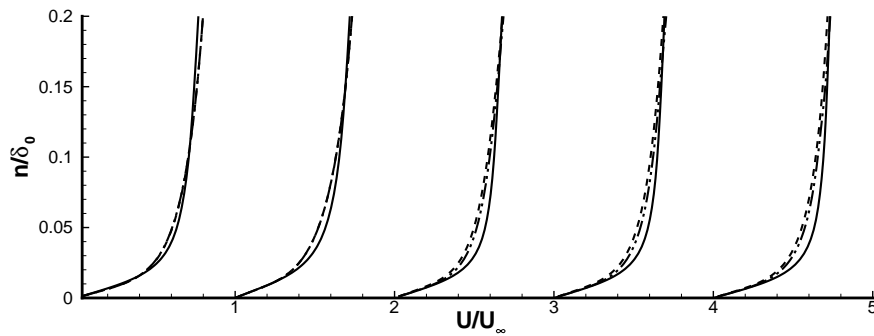


Figure 14. Concave boundary layer: Mean streamwise velocity profiles plotted in wall-normal coordinate normalized by 99% boundary layer thickness at the inflow. For line legend, see figure 13.

cific conclusions drawn based on the observations:

- At the onset of concave curvature, the effect of adverse pressure gradient is predominant producing decreased levels of skin friction.
- The effect of concave curvature shows largest effect on the wall-normal component of the Reynolds stress component. The budgets of v^2 component shows that the contribution to production term increases as the flow moves farther into the concave curvature.
- The effect of curvature is seen to be largest on the turbulent transport term in the TKE budgets, in agreement with the earlier DNS observations.
- Bifurcation analysis based curvature correction responds in the right direction to the combined effects of pressure gradient and concave curvature, but there is still scope for further improvement.

Future work involves *a priori* analysis of the LES data with an objective to further assess and improve the RANS models.

Acknowledgments

This work used computational resources of Stampede under the Extreme Science and Engineering Discovery Environment (XSEDE), which is supported by National Science Foundation Grant No. OCI-1053575.

References

- [1] R.N. Meroney, and P. Bradshaw, *Turbulent boundary-layer growth over a longitudinally curved surface*, AIAA Journal 13 (1975), pp. 1448–1453.
- [2] P.H. Hoffmann, K.C. Muck, and P. Bradshaw, *The effect of concave surface curvature on turbulent boundary layers*, J. Fluid Mech. 161 (1985), pp. 371–403.
- [3] R.S. Barlow, and J.P. Johnston, *Structure of a turbulent boundary layer on a concave surface*, J. Fluid Mech. 191 (1988), pp. 137–176.
- [4] P.L. Johnson, and J.P. Johnston, *The effects of grid-generated turbulence on flat and concave turbulent boundary layers*, Report No. MD-53, Dept. of Mech. Eng., Stanford University, 1989.
- [5] T.S. Lund, and P. Moin, *Large-eddy simulation of a concave wall boundary layer*, Int. J. Heat Fluid Flow 17 (1996), pp. 290–295.
- [6] S.K. Arolla, and P.A. Durbin, *Modeling rotation and curvature effects within scalar eddy viscosity model framework*, Int. J. Heat Fluid Flow 39 (2013), pp. 78–89.
- [7] A.G.L. Holloway, D.C. Roach, and H. Akbary, *Combined effects of favourable pressure gradient and streamline curvature on uniformly sheared turbulence*, J. Fluid Mech. 526 (2005), pp. 303–336.
- [8] A.C. Schwarz, M.W. Plesniak, and S.N.B. Murthy, *Response of turbulent boundary layers to multiple strain rates*, J. Fluid Mech. 458 (2002), pp. 333–377.
- [9] P.R. Bandyopadhyay, and A. Ahmed, *Turbulent boundary layers subjected to multiple curvatures and pressure gradients*, J. Fluid Mech. 246 (1993), pp. 503–527.
- [10] G.M. Laskowski, and P.A. Durbin, *Direct numerical simulations of turbulent flow through a stationary and rotating infinite serpentine passage*, Phys. Fluids 19 (2007).
- [11] A.S. Lopes, U. Piomelli, and J.M.L.M. Palma, *Large-eddy simulation of the flow in an S-duct*, J. Turbulence 7 (2009).
- [12] R.D. Moser, and P. Moin, *The effects of curvature in wall-bounded turbulent flows*, J. Fluid Mech. 175 (1987), pp. 479–510.
- [13] M.P. Schultz, and R.J. Volino, *Effects of concave curvature on boundary layer transition under high free-stream turbulence conditions*, ASME J. Fluids Eng. 125 (2003), pp. 18–27.
- [14] M.D. Kestoras, and T.W. Simon, *Effects of free-stream turbulence intensity on a boundary layer recovering from concave curvature effects*, ASME J. Turbomach 117 (1995), pp. 240–247.
- [15] X. Wu, and P.A. Durbin, *Boundary layer transition induced by periodic wakes*, ASME J. Turbomach 122 (1998), pp. 442–449.
- [16] L.U. Schrader, L. Brandt, and T. Zaki, *Receptivity, instability and breakdown of Goertler flow*, J. Fluid Mech. 682 (2011), pp. 362–396.
- [17] S.K. Arolla, and P.A. Durbin, *Generating inflow turbulence for eddy simulation of turbomachinery flows*, in *52nd AIAA Aerospace Sciences Meeting, National Harbor, Maryland, 2014*.
- [18] M. Germano, U. Piomelli, P. Moin, and W.H. Cabot, *A dynamic subgrid-scale eddy viscosity model*, Phys. Fluids A 3 (1991), p. 1760.
- [19] D.K. Lilly, *A proposed modification of the Germano subgrid-scale closure method*, Phys. Fluids A 4 (1992), p. 633.

- [20] P. Spalart, M. Strelets, and A. Travin, *Direct numerical simulation of large-eddy-break-up devices in a boundary layer*, Int. J. Heat Fluid Flow 27 (2006), pp. 902–910.
- [21] J. Jewkes, Y. Chung, and P. Carpenter, *Modification to a turbulent inflow generation method for boundary-layer flows*, AIAA Journal 49 (2011), pp. 247–250.
- [22] D.B. DeGraaff, and J.K. Eaton, *Reynolds-number scaling of the flat-plate turbulent boundary layer*, J. Fluid Mech. 422 (2000), pp. 319–346.
- [23] P. Spalart, *Direct simulation of a turbulent boundary layer up to $R_\theta = 1410$* , J. Fluid Mech. 187 (1988), pp. 61–98.
- [24] P. Bradshaw, *Effects of streamline curvature on turbulent flow*, AD0768316, AGARDograph report, 1973.
- [25] V.C. Patel, and Sotiropoulos, *Longitudinal curvature effects in turbulent boundary layers*, Prog. Aerosp. Sci. 33 (1997), pp. 1–70.
- [26] F.R. Menter, *Two-equation eddy-viscosity turbulence models for engineering applications*, AIAA Journal 32 (1994), pp. 269–289.
- [27] M.L. Shur, M.K. Strelets, A.K. Travin, and P. Spalart, *Turbulence modeling in rotating and curved channels: Assessing the Spalart-Shur correction*, AIAA Journal 38 (2000), pp. 784–792.

Appendix A. A variant of the recycling and rescaling method

The steps involved in the new variant of recycling and rescaling method of inflow generation algorithm are:

- (1) Extract the velocity field, $u(x_r, y, z, t)$, at the recycling plane located at x_r and project on to the inflow boundary (see figure A1).

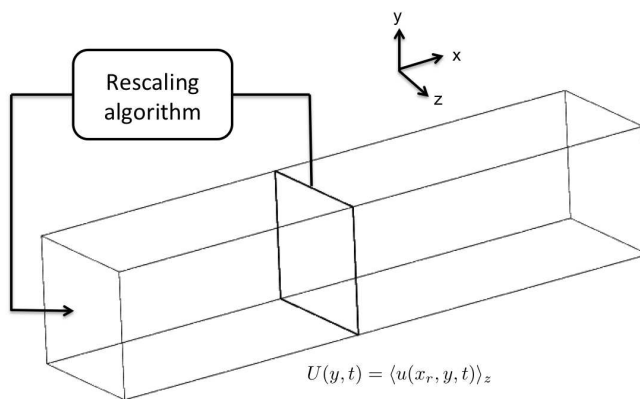


Figure A1. A schematic of the computational domain used for flat plate turbulent boundary layer simulation. The recycling plane is located at $x_r = 5\delta_0$ from the inflow boundary.

- (2) Perform spanwise averaging to be $U(y, t) = \langle u(x, y, t) \rangle_z$. A simple indexing algorithm is used for the averaging. It involves looping over all the faces and index faces with the same wall-normal coordinate. Since the recycling plane is fixed, this indexing can be stored at the preprocessing step itself and reused at each timestep.
- (3) Find the freestream velocity $U_\infty = U(y_{max}, t)$.
- (4) Integrate the velocity profile to compute the momentum thickness:

$$\theta_r = \int_0^{y_{max}} \frac{U(y, t)}{U_\infty} \left(1 - \frac{U(y, t)}{U_\infty} \right) dy \quad (\text{A1})$$

- (5) Compute the rescaling factor, $\gamma = \theta_r / \theta_{in}$, where θ_{in} is the desired momentum thickness at the inflow.
- (6) Rescale only the x-component of the velocity field:

$$u(x_{in}, y, z, t) = u(x_r, y\gamma, z, t - \Delta t) \quad (\text{A2})$$

where $t - \Delta t$ means the velocity from the previous time step is used for convenience. A linear interpolation is used to compute velocity at the rescaled y-coordinate.

- (7) Apply spanwise mirroring to disorganize unphysical structures which would otherwise be recycled and take much time to be dampened by the spanwise diffusion.

$$\begin{aligned} u(x_{in}, y, z, t) &= u(x_{in}, y, \Delta z - z, t) \\ v(x_{in}, y, z, t) &= v(x_{in}, y, \Delta z - z, t) \\ w(x_{in}, y, z, t) &= -w(x_{in}, y, \Delta z - z, t) \end{aligned} \quad (\text{A3})$$

where Δz is considered to be equal to the spanwise period. Note that w has to be negative to ensure spatial coherence once mirrored [21].

- (8) Check for constant mass flow rate at the inflow by verifying the bulk velocity.

Appendix B. Summary of RANS models

B.1. SST $k - \omega$ model

The SST variant of $k - \omega$ [26] is used as a baseline turbulence model. It is of the following form

$$\frac{\partial k}{\partial t} + u_j \frac{\partial k}{\partial x_j} = \mathcal{P} - D_k + \frac{\partial}{\partial x_j} \left[\left(\nu + \frac{\nu_T}{\sigma_k} \right) \frac{\partial k}{\partial x_j} \right] \quad (\text{B1})$$

where $D_k = \beta^* k \omega$ and $\mathcal{P} = \nu_t \mathcal{S}^2$.

$$\frac{\partial \omega}{\partial t} + u_j \frac{\partial \omega}{\partial x_j} = \frac{\gamma}{\nu_T} \mathcal{P} - D_\omega + \frac{\partial}{\partial x_j} \left[\left(\nu + \frac{\nu_T}{\sigma_\omega} \right) \frac{\partial \omega}{\partial x_j} \right] + CD_\omega \quad (\text{B2})$$

where $D_\omega = \beta \omega^2$ and CD_ω is the cross-diffusion term. The eddy viscosity, with no accounting for curvature effects is $\nu_T = C_\mu k / \omega$ with $C_\mu = 1$.

B.2. SST $k - \omega$ with bifurcation analysis based curvature correction

The curvature correction [6] is applied to the eddy viscosity coefficient as $\nu_T = C_\mu^* k / \omega$, where

$$\begin{aligned} A &= C_\mu \left(\alpha_1 (|\eta_3| - \eta_3) + \sqrt{1 - \min(\alpha_2 \eta_3, 0.99)} \right)^{-1} \\ C_\mu^* &= \min(2.5, A) \end{aligned} \quad (\text{B3})$$

We selected $\alpha_1 = 0.04645$ and $\alpha_2 = 0.25$ based on the bifurcation diagram of RSMs. The invariants used in the models are

$$\eta_1 = S_{ij} S_{ij} T^2; \quad \eta_2 = \Omega_{ij}^{mod} \Omega_{ij}^{mod} T^2; \quad \eta_3 = \eta_1 - \eta_2 \quad (\text{B4})$$

The coefficient $C_r = 2$.

The time scale used is $T = \max(T_1, T_3)$ where

$$T_1 = \frac{1}{\beta^* \omega}; \quad T_2 = 6 \sqrt{\frac{\nu}{\beta^* k \omega}}; \quad T_3 = (T_1^n T_2)^{1/n+1} \quad (\text{B5})$$

with $n = 1.625$.

The definitions of the rate of strain and rate of rotation are:

$$S_{ij} = \frac{1}{2}(\partial_j U_i + \partial_i U_j); \quad \Omega_{ij}^{mod} = \Omega_{ij}^A + (C_r - 1)W_{ij}^A \quad (\text{B6})$$

where $\Omega_{ij}^A = \Omega_{ij}^{rel} + \Omega_{ij}^F$ with $\Omega_{ij}^{rel} = \frac{1}{2}(\partial_i U_j - \partial_j U_i)$ and $\Omega_{ij}^F = -\epsilon_{ijk} \Omega_k^F$. Ω_k^F is the angular frame velocity about the x_k -axis. The rotation and curvature are unified through W_{ij}^A . In 2D, this is equivalent to the Spalart-Shur tensor [27]:

$$\Omega^{SS} \equiv \Omega^F - \frac{\mathbf{S} \cdot D_t \mathbf{S} - D_t \mathbf{S} \cdot \mathbf{S}}{2|\mathbf{S}|^2} \quad (\text{B7})$$

Note that for the curvature-corrected RANS results presented in this article, the above 2D form of Spalart-Shur tensor is used.